ChemComm

COMMUNICATION

View Article Online
View Journal | View Issue

Check for updates

Cite this: *Chem. Commun.*, 2019, 55, 2493

Received 14th December 2018, Accepted 25th January 2019

DOI: 10.1039/c8cc09924c

rsc.li/chemcomm

Nanosheet-based $Nb_{12}O_{29}$ hierarchical microspheres for enhanced lithium storage†

Renjie Li,[ab] Xiangzhen Zhu,[b] Qingfeng Fu,[b] Guisheng Liang,[b] Yongjun Chen,[b] Lijie Luo,[b] Mengyao Dong,[cd] Qian Shao,[e] Chunfu Lin,*[ab] Renbo Wei*[f] and Zhanhu Guo*[c]

Conductive $Nb_{12}O_{29}$ hierarchical microspheres with nanosheet shells were synthesized based on a hydrothermal process and a high-temperature hydrogen reduction treatment. The obtained materials demonstrated comprehensively good electrochemical properties, including a significant pseudocapacitive contribution, safe operating potential, high reversible capacity, superior initial coulombic efficiency, increased rate capability, and durable cycling stability.

Rechargeable lithium-ion batteries (LIBs) have been widely used as power supplies in portable electronics, and they will hopefully be utilized in large-scale energy-storage applications, such as electric vehicles.[1–5] Current LIBs predominantly use intercalating graphite as the anode material owing to its high practical capacity and economic concerns. However, graphite suffers from notable safety perils and an unsatisfactory rate capability, which do not meet the requirements for future large-scale applications.[6] To handle these problems, titanium- and niobium-based oxides are of tremendous interest due to their safe operating potentials (Ti^{3+}/Ti^{4+}, Nb^{3+}/Nb^{4+} and Nb^{4+}/Nb^{5+}) ranging from 1.0 to 2.0 V. This prevents not only the reduction of electrolyte but also the formation and growth of solid electrolyte interface (SEI) layers/lithium dendrites.[7,8] Compared with titanium-based oxides, niobium-based oxides have drawn increasing interest by virtue of their higher reversible capacities giving rise to two-electron transfer *per* niobium.[9–12] However, niobium-based oxides generally show very poor electronic conductivities owing to the highest oxidation states of niobium and heteroatom, limiting their rate capabilities.

Recently, $Nb_{12}O_{29}$ (*i.e.*, $Nb^{IV}{}_2Nb^{V}{}_{10}O_{29}$) has been demonstrated to show a good rate capability owing to the 4d electrons in Nb^{4+} ions ($4d^1$).[13] The electronic-conductivity test and first-principles calculations in the previous research confirmed the conductive nature of $Nb_{12}O_{29}$.[13] In order to obtain better electrochemical performance, decreasing the particle size is one of the most persuasive approaches since large effective areas of active materials should induce short Li^+ and electron transport distances.[14] To the best of our knowledge, no research related to nanostructured $Nb_{12}O_{29}$ has so far been reported.

In this work, nanosheet-based $Nb_{12}O_{29}$ hierarchical microspheres (n-$Nb_{12}O_{29}$) were fabricated through a high-temperature hydrogen reduction of nanosheet-based Nb_2O_5 hierarchical microspheres (n-Nb_2O_5), which were synthesized based on a hydrothermal method. The 4d electrons caused by the Nb^{4+} ions benefited the rate capability of $Nb_{12}O_{29}$. Besides this merit, the nanosheet-based hierarchical microspheres made the whole nanosheets efficiently participate in the electrochemical reaction. The hierarchical structure and presence of nanosheets on the surface enlarged the contact area and shortened the Li^+ diffusion lengths. These features led to excellent electrochemical properties of n-$Nb_{12}O_{29}$, including a significant pseudocapacitive contribution, superior initial coulombic efficiency, increased reversible capacity, safe operating potential, superior rate capability, and excellent cycling stability.

The phase purity and crystal structures of n-Nb_2O_5 and n-$Nb_{12}O_{29}$ were examined by powder X-ray diffraction (XRD). The XRD pattern of n-Nb_2O_5 (Fig. 1a) depicts one set of diffraction peaks matching well with orthorhombic Nb_2O_5 (JCPDS card No. 27-1313). After 12 h of hydrogen reduction treatment, oxygen loss

[a] *Institute of Materials for Energy and Environment, School of Materials Science and Engineering, Qingdao University, Qingdao 266071, China. E-mail: linchunfu@qdu.edu.cn*
[b] *State Key Laboratory of Marine Resource Utilization in South China Sea, College of Materials and Chemical Engineering, Hainan University, Haikou 570228, China*
[c] *Integrated Composites Laboratory (ICL), Department of Chemical & Biomolecular Engineering, University of Tennessee, Knoxville, TN 37996, USA. E-mail: zguo10@utk.edu, nanomaterials2000@gmail.com*
[d] *Key Laboratory of Materials Processing and Mold (Zhengzhou University), Ministry of Education; National Engineering Research Center for Advanced Polymer Processing Technology, Zhengzhou University, Zhengzhou 450002, China*
[e] *College of Chemical and Environmental Engineering, Shandong University of Science and Technology, Qingdao, Shandong, 266590, China*
[f] *Research Branch of Advanced Functional Materials, School of Materials and Energy, University of Electronic Science and Technology of China, Chengdu, 611731, China. E-mail: weirb10@uestc.edu.cn*

† Electronic supplementary information (ESI) available: Experimental details; discharging–charging profiles of n-Nb_2O_5 at different current rates (Fig. S1), cycling stability of n-Nb_2O_5 at 10C over 500 cycles (Fig. S2), and comparison of the rate capability of n-$Nb_{12}O_{29}$ with previously reported niobium-based anode materials (Table S1). See DOI: 10.1039/c8cc09924c

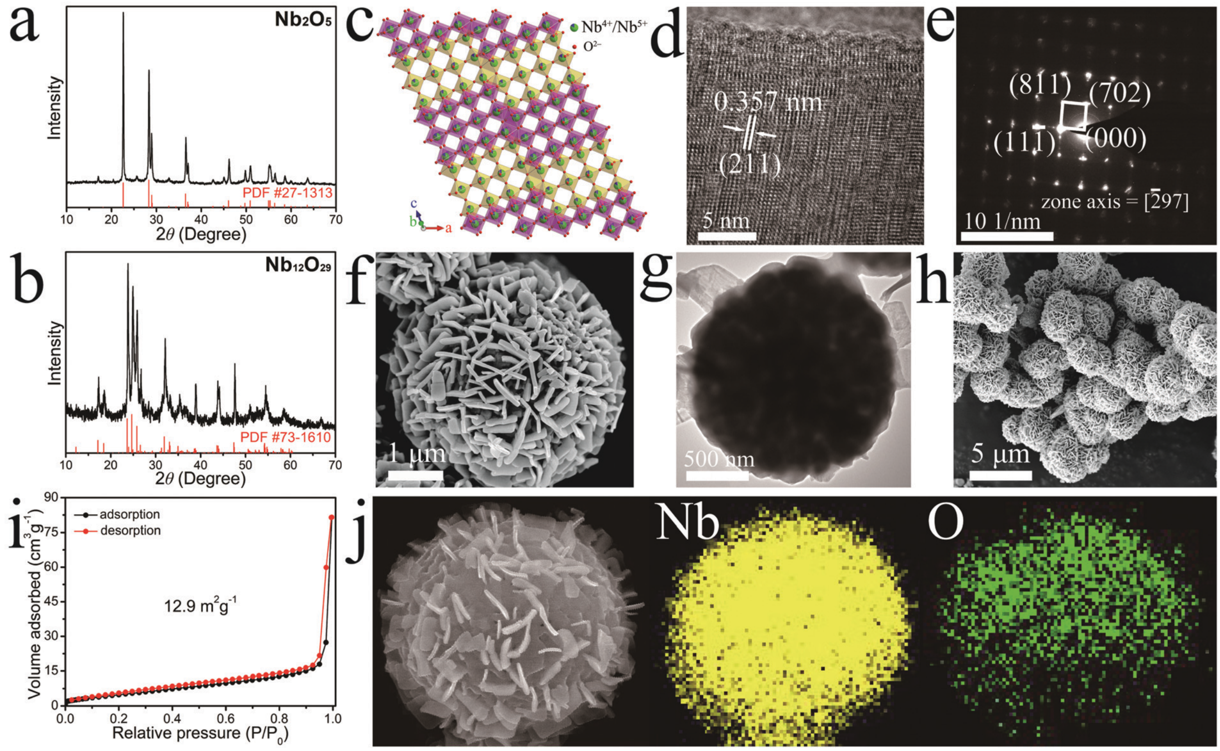

Fig. 1 XRD patterns of (a) n-Nb_2O_5 and (b) n-$Nb_{12}O_{29}$. (c) Crystal structure of n-$Nb_{12}O_{29}$. (d) HRTEM image, (e) SAED pattern, (f) high-magnification FESEM image, and (g) TEM image of n-$Nb_{12}O_{29}$. (h) Low-magnification FESEM image of n-Nb_2O_5. (i) Nitrogen adsorption–desorption isotherms of n-$Nb_{12}O_{29}$. (j) EDX mapping images of n-$Nb_{12}O_{29}$.

transformed Nb_2O_5 into $Nb_{12}O_{29}$. Fig. 1b reveals that all observed peaks match well with those of the monoclinic $Nb_{12}O_{29}$ (JCPDS card No. 73-1610), indicating that n-Nb_2O_5 was completely transformed into n-$Nb_{12}O_{29}$ after the reduction process. It is noteworthy that orthorhombic Nb_2O_5 was obtained at 700 °C but monoclinic $Nb_{12}O_{29}$ required 750 °C and H_2/Ar treatment to be formed. Monoclinic $Nb_{12}O_{29}$ shows a 3 × 4 Wadsley–Roth crystal structure, constructed by edge- and/or corner-sharing octahedra to guarantee the great structural stability of $Nb_{12}O_{29}$ (Fig. 1c). The positive ions are formed by Nb^{5+} and Nb^{4+} ions at an atomic ratio of 5 : 1, located in the centers of the octahedra. The crystal structure was also verified by high-resolution transmission electron microscopy (HRTEM) and selected-area electron diffraction (SAED) characterization. Fig. 1d depicts a lattice distance of 0.357 nm, corresponding to the (211) crystallographic plane of $Nb_{12}O_{29}$. The obtained SAED pattern of $Nb_{12}O_{29}$ in Fig. 1e agrees well with the monoclinic Wadsley–Roth crystal structure (*A*2/*m* space group).

The morphology, microstructure and particle size of n-$Nb_{12}O_{29}$ were examined by high-magnification field emission scanning electron microscopy (FESEM) and TEM images (Fig. 1f and g). Numerous microspheres with an average diameter of approximately 3 μm are observed. The shell formed by nanosheets with a thickness of approximately 50 nm effectively ensured the architectural stability. The low-magnification FESEM image of n-Nb_2O_5 reveals the same morphology as n-$Nb_{12}O_{29}$ (Fig. 1h), indicating that the morphology remained unchanged and no aggregation was formed after the high-temperature hydrogen reduction. Therefore, the long calcination did not noticeably alter the morphology or particle size. The Brunauer–Emmett–Teller (BET) specific surface area of n-$Nb_{12}O_{29}$ was estimated at 12.9 $m^2\ g^{-1}$ (Fig. 1i), which is much larger than that of micron-sized $Nb_{12}O_{29}$ (m-$Nb_{12}O_{29}$) in the previous work (0.9 $m^2\ g^{-1}$).[13] This should lead to better electrochemical properties owing to the large interfacial area between the electroactive material and electrolyte, which shortens the Li^+ and electron transport lengths. To get the elemental distributions, energy-dispersive X-ray spectroscopy (EDX) was also used. The contents of both Nb and O elements are uniformly distributed in the mapping images of n-$Nb_{12}O_{29}$ (Fig. 1j), confirming the pure $Nb_{12}O_{29}$ phase.

To gain better understanding of the nanomaterial influences on the electrochemical kinetics, an electrochemical impedance spectroscopy (EIS) measurement of n-$Nb_{12}O_{29}$ was performed, and the resulting Nyquist plot is shown in Fig. 2a. Based on the corresponding equivalent circuit model (inset of Fig. 2a), the R_1/CPE_1 pair stands for the synergistic effect of Li^+ desolvation, electron transfer and adsorption, R_2/CPE_2 refers to the Li^+ insertion at the surface, W is the Warburg resistance, representing the Li^+ diffusion in the $Nb_{12}O_{29}$ lattice, and R_b embodies the Ohmic resistance of the cell.[15] The fitted R_1 and R_2 values of n-$Nb_{12}O_{29}$ were estimated to be at 80 and 399 Ω, respectively. By comparison, the corresponding values of m-$Nb_{12}O_{29}$ are 397 and 824 Ω.[13] The small resistances of n-$Nb_{12}O_{29}$ indicate its ability to perform quick Li^+ adsorption/desolvation, fast electron transfer, and rapid Li^+ insertion at the surface. These features undoubtedly led to better electrochemical kinetics.

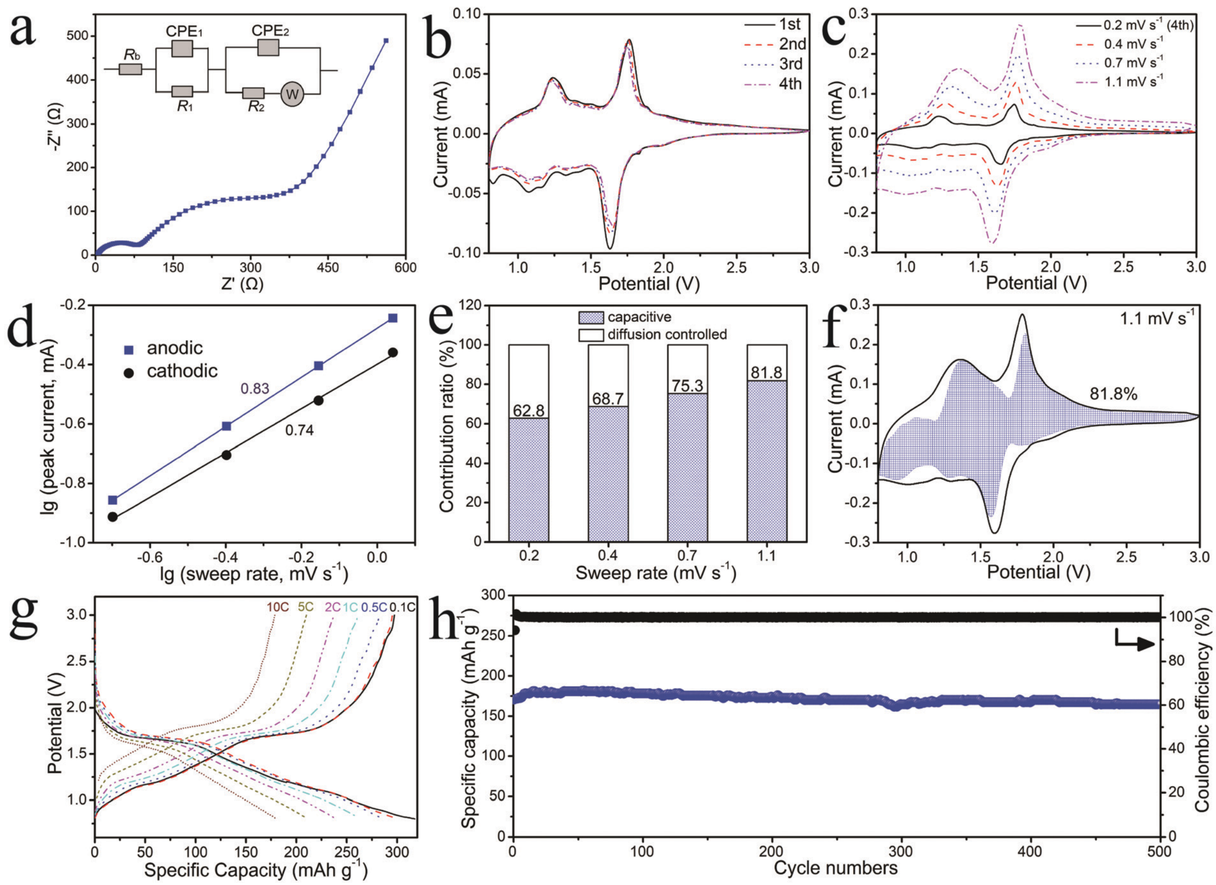

Fig. 2 Electrochemical properties of n-$Nb_{12}O_{29}$: (a) Nyquist plot and selected equivalent circuit, (b) CV curves at 0.2 mV s^{-1}, (c) CV curves at different sweep rates, (d) plots of log(current) *vs.* log(sweep rate), (e) pseudocapacitive contribution ratios at different sweep rates, (f) pseudocapacitive contribution at 1.1 mV s^{-1}, (g) discharging–charging profiles at different current rates, and (h) cycling stability over 500 cycles at 10C.

To further clarify the redox kinetics of n-$Nb_{12}O_{29}$, cyclic voltammetry (CV) tests were implemented at a slow sweep rate of 0.2 mV s^{-1} within 3.0–0.8 V for four cycles (Fig. 2b). The cathodic branch in the first cycle appears marginally different from subsequent curves. This could be caused by irreversible polarization processes occurring during the first scan.[16] After that, the scanning curves have a great coincidence, advising high electrochemical reversibility and good cycling stability of n-$Nb_{12}O_{29}$. The second scan shows a pair of sharp cathodic/anodic peaks at 1.63/1.75 V and a wide bump within 1.5–0.8 V, vesting in the reduction/oxidation reactions from the Nb^{4+}/Nb^{5+} and Nb^{3+}/Nb^{4+} redox couples, respectively.

To further explore the intercalation pseudocapacitive behavior of n-$Nb_{12}O_{29}$, CV curves were afterward recorded at higher sweep rates (Fig. 2c). The intercalation pseudocapacitive behavior was calculated and analyzed by a previous study.[5,9] The slope values of the log(current)–log(sweep rate) splashes of the cathodic and anodic processes respectively reach as large as 0.74 and 0.83 (Fig. 2d). These large values indicate dominant pseudocapacitive control in the electrochemical reaction.[17–19] Fig. 2e and f show that the pseudocapacitive contributions in n-$Nb_{12}O_{29}$ reach 62.8, 68.7, 75.3 and 81.8% at 0.2, 0.4, 0.7 and 1.1 mV s^{-1}, respectively. These large percentages reveal its excellent intercalation pseudocapacitive performance in both slow and fast sweep rates. The significant pseudocapacitive behavior of n-$Nb_{12}O_{29}$ can be attributed to its open crystal structure, the existence of unpaired Nb^{4+} state, and large specific surface area caused by the hierarchical microspheres. This desirable behavior should be one of the decisive factors contributing to the outstanding rate capability of n-$Nb_{12}O_{29}$.

To examine the Li^+-storage performance of n-$Nb_{12}O_{29}$, galvanostatic discharging–charging measurements were performed at 0.1C, 0.5C, 1C, 2C, 5C and 10C, and the results are gathered in Fig. 2g. Each curve of n-$Nb_{12}O_{29}$ at 0.1C displays (i) a first sloping line from the initial potential (or 3.0 V) to ~1.7 V, (ii) a short plateau within 1.7–1.6 V, and (iii) a long steep line from 1.6 V until 0.8 V. These three steps could be attributed to solid-solution reaction → double-phase transformation → another solid-solution reaction.[20] The discharging–charging curves are consistent with the CV graphic patterns illustrated in Fig. 2b and c. The calculated average operating potential (~1.61 V) from the energy–capacity relationship is in good accordance with the sharp CV cathodic and anodic peaks. The high operating potential prevented the formation of lithium dendrites and the decomposition of the electrolyte, thereby ensuring great safety behavior.

At a small current rate of 0.1C, n-$Nb_{12}O_{29}$ delivered a high reversible capacity reaching 297 mA h g^{-1} and an increased initial coulombic efficiency of up to 94.1%. At 0.5C, 1C, 2C and 5C, n-$Nb_{12}O_{29}$ maintained high capacities of 282, 261, 238 and 210 mA h g^{-1}, respectively. When measured at a large current rate of 10C, which took only six minutes to fully discharge/charge, n-$Nb_{12}O_{29}$ still provided 179 mA h g^{-1}. This value is about 60.0% of the capacity obtained at 0.1C. Clearly, n-$Nb_{12}O_{29}$ exhibited a higher rate capability than n-Nb_2O_5 (125 mA h g^{-1} at 10C, Fig. S1, ESI†) and m-$Nb_{12}O_{29}$ (165 mA h g^{-1} at 10C).[13] In fact, the rate capability of n-$Nb_{12}O_{29}$ is among the best results reported on niobium-based anode materials (Table S1, ESI†).[21–31] This outstanding rate capability of n-$Nb_{12}O_{29}$ can be associated with its large surface contact area, short Li^+ and electron transport lengths, high electronic conductivity, and significant pseudocapacitive behavior.

The cycling stability of n-$Nb_{12}O_{29}$ at 10C was examined, and the results are noted in Fig. 2h. After a continuous measurement for 500 cycles, small capacity loss of only 3.5% was achieved for n-$Nb_{12}O_{29}$ and is smaller than that of n-Nb_2O_5 (capacity loss of 21.0%, Fig. S2, ESI†) and m-$Nb_{12}O_{29}$ (capacity loss of 7.0%).[13] The initial coulombic efficiency of 94.2% is in accordance with the initial discharging–charging curves shown in Fig. 2g. After the initial cycle, the coulombic efficiency always maintained at 100%. This advanced cycling stability of n-$Nb_{12}O_{29}$ could be attributed to not only its intercalating nature but also the nanosheet-based hierarchical microspheres without aggregation.

In summary, nanosheet-based $Nb_{12}O_{29}$ hierarchical microspheres were synthesized by novel high-temperature hydrogen reduction of hydrothermal nanosheet-based Nb_2O_5 hierarchical microspheres. This novel $Nb_{12}O_{29}$ material showed an average sphere diameter of ∼3 μm and shell thickness of ∼50 nm. The nanosheets, restricted self-aggregation, and conductive Nb^{4+} ions resulted in facile charge transport, fast electrochemical kinetics, and significant pseudocapacitive behavior. Consequently, it exhibited outstanding electrochemical properties in terms of a safe operating potential (∼1.61 V), high reversible capacity (297 mA h g^{-1} at 0.1C), increased initial coulombic efficiency (94.1%), admirable rate capability (179 mA h g^{-1} at 10C), and excellent cycling stability (3.5% loss at 10C over 500 cycles). Overall, these findings demonstrate the feasibility of using the nanosheet-based $Nb_{12}O_{29}$ hierarchical microspheres as a promising anode material for superior lithium storage.

This work was financially supported by the National Natural Science Foundation of China (51762014), the Taishan Scholar Program of Shandong Province, and the World-Class Discipline Program and the Taishan Scholar's Advantageous and Distinctive Discipline Program of Shandong Province.

Conflicts of interest

There are no conflicts to declare.

Notes and references

1 (*a*) K. Kang, Y. S. Meng, J. Bréger, C. P. Grey and G. Ceder, *Science*, 2006, **311**, 977; (*b*) L. Yan, H. Wang, D. Huang and H. Luo, *Eng. Sci.*, 2018, **1**, 4–20, DOI: 10.30919/es.180318.
2 (*a*) M. Armand and J. M. Tarascon, *Nature*, 2008, **451**, 652; (*b*) B. Kang and G. Ceder, *Nature*, 2009, **458**, 190.
3 (*a*) M. Idrees, S. Batool and J. Kong, *et al.*, *Electrochim. Acta*, 2019, **296**, 925–937; (*b*) Q. Hou, J. Ren and H. Chen, *et al.*, *ChemElectroChem*, 2018, **5**, 726–731; (*c*) X. Zhao, P. Yang and L. Yang, *et al.*, *ES Mater. Manuf.*, 2018, **1**, 67–71, DOI: 10.30919/esmm5f109.
4 (*a*) B. Dunn, H. Kamath and J. M. Tarascon, *Science*, 2011, **334**, 928; (*b*) Z. Qu, M. Shi and H. Wu, *et al.*, *J. Power Sources*, 2019, **410–411**, 179–187; (*c*) C. Lin, H. Hu and C. Cheng, *et al.*, *Electrochim. Acta*, 2018, **260**, 65–72.
5 (*a*) V. Etacheri, R. Marom, R. Elazari, G. Salitra and D. Aurbach, *Energy Environ. Sci.*, 2011, **4**, 3243; (*b*) C. Hou, Z. Tai, L. Zhao, Y. Zhai and Y. Hou, *et al.*, *J. Mater. Chem. A*, 2018, **6**, 9723–9736.
6 S. S. Zheng, *J. Power Sources*, 2006, **161**, 1385.
7 C. F. Lin, X. Y. Fan, Y. L. Xin, F. Q. Cheng, M. O. Lai, H. H. Zhou and L. Lu, *J. Mater. Chem. A*, 2014, **2**, 9982.
8 L. Hu, L. J. Luo, L. F. Tang, C. F. Lin, R. J. Li and Y. J. Chen, *J. Mater. Chem. A*, 2018, **6**, 9799.
9 C. Yang, S. Yu, C. F. Lin, F. Lv, S. Q. Wu, Y. Yang, W. Wang, Z. Z. Zhu, J. B. Li, N. Wang and S. J. Guo, *ACS Nano*, 2017, **11**, 4217.
10 (*a*) X. M. Lou, Z. H. Xu and Z. B. Luo, *et al.*, *Electrochim. Acta*, 2017, **245**, 482; (*b*) X. Zhao, P. Yang and L. Yang, *et al.*, *ES Mater. Manuf.*, 2018, **1**, 67–71.
11 B. K. Guo, X. Q. Yu, X. G. Sun, M. F. Chi, Z. A. Qiao, J. Liu, Y. S. Hu, X. Q. Yang, J. B. Goodenough and S. Dai, *Energy Environ. Sci.*, 2014, **7**, 2220.
12 K. J. Griffith, K. M. Wiaderek, G. Cibin, L. E. Marbella and C. P. Grey, *Nature*, 2018, **559**, 556.
13 R. J. Li, Y. Qin, X. Liu, L. Yang, C. F. Lin, R. Xia, S. W. Lin, Y. J. Chen and J. B. Li, *Electrochim. Acta*, 2018, **266**, 202.
14 S. F. Lou, Y. L. Ma, X. Q. Cheng, J. L. Gao, Y. Z. Gao, P. J. Zuo, C. Y. Du and G. P. Yin, *Chem. Commun.*, 2015, **51**, 17293.
15 M. Nakayama, H. Ikuta, Y. Uchimoto and M. Wakihara, *J. Phys. Chem. B*, 2003, **107**, 10603.
16 X. Lu, Z. L. Jian, Z. Fang, L. Gu, Y. S. Hu, W. Chen, Z. X. Wang and L. Q. Chen, *Energy Environ. Sci.*, 2011, **4**, 2638.
17 V. Augustyn, J. Come and M. Lowe, *et al.*, *Nat. Mater.*, 2013, **12**, 518.
18 H. S. Kim, J. B. Cook, H. Lin, J. S. Ko, S. H. Tolbert, V. Ozolins and B. Dunn, *Nat. Mater.*, 2017, **16**, 454.
19 B. H. Deng, T. Y. Lei, W. H. Zhu, L. Xiao and J. P. Liu, *Adv. Funct. Mater.*, 2018, **28**, 1704330.
20 X. Y. Wu, J. Miao, W. Z. Han, Y. S. Hu, D. F. Chen, J. S. Lee, J. Kim and L. Q. Chen, *Electrochem. Commun.*, 2012, **25**, 39.
21 X. M. Lou, Q. F. Fu, J. Xu, X. Liu, C. F. Lin, J. X. Han, Y. P. Luo, Y. J. Chen, X. Y. Fan and J. B. Li, *ACS Appl. Nano Mater.*, 2018, **1**, 183.
22 X. Lou, C. Lin, Q. Luo, J. Zhao, B. Wang, J. Li, Q. Shao, X. Guo, N. Wang and Z. Guo, *ChemElectroChem*, 2017, **4**, 3171.
23 C. F. Lin, G. Z. Wang, S. W. Lin, J. B. Li and L. Lu, *Chem. Commun.*, 2015, **51**, 8970.
24 C. F. Lin, S. Yu, H. Zhao, S. Q. Wu, G. Z. Wang, L. Yu, Y. F. Li, Z. Z. Zhu, J. B. Li and S. W. Lin, *Sci. Rep.*, 2015, **5**, 17836.
25 C. F. Lin, S. Yu, S. Q. Wu, S. W. Lin, Z. Z. Zhu, J. B. Li and L. Lu, *J. Mater. Chem. A*, 2015, **3**, 8627.
26 J. L. Gao, X. Q. Cheng, S. F. Lou, Y. L. Ma, P. J. Zuo, C. Y. Du, Y. Z. Gao and G. P. Yin, *J. Alloys Compd.*, 2017, **728**, 534.
27 K. Tang, X. K. Mu, P. A. van Aken, Y. Yu and J. Maier, *Adv. Energy Mater.*, 2013, **3**, 49.
28 L. Hu, C. F. Lin, C. H. Wang, C. Yang, J. B. Li, Y. J. Chen and S. W. Lin, *Funct. Mater. Lett.*, 2016, **9**, 1642004.
29 S. Lou, X. Chen and J. Gao, *et al.*, *Energy Storage Mater.*, 2018, **11**, 57.
30 Q. F. Fu, J. R. Hou, R. H. Lu, C. F. Lin, Y. Ma, J. B. Li. and Y. J. Chen, *Mater. Lett.*, 2018, **214**, 60.
31 W. Mao, K. Liu and G. Gao, *et al.*, *Electrochim. Acta*, 2017, **353**, 396.